CFD simulation of a Spouted Bed: comparison between the Discrete Element Method (DEM) and the Two Fluid Method (TFM)

Cristina Moliner[1*], Filippo Marchelli[2], Nayia Spanachi[3], Alfonso Martinez-Felipe[3], Barbara Bosio[1] and Elisabetta Arato[1]

[1] *University of Genova, Department of Civil, Chemical and Environmental Engineering, Via Opera Pia 15A, 16145 Genova (Italy)*

[2] *Free University of Bozen-Bolzano, Faculty of Science and Technology, Piazza Università 5, 39100 Bolzano (Italy)*

[3] *Chemical and Materials Engineering Group, School of Engineering, University of Aberdeen, King's College, Aberdeen (United Kingdom) AB24 3UE, UK*

*Corresponding author: cristina.moliner@edu.unige.it

Highlights

- A prismatic spouted bed was modelled using CFD.

- A comparison between discrete element method (CFD-DEM) and two fluid model (CFD-TFM) was performed.

- Results in terms of accuracy and computational effort were evaluated for each approach.

- CFD-DEM provides a better prediction of maximum particle velocity.

- CFD-TFM predicts better the height of the fountain.

Abstract

A spouted bed was simulated through two Computational Fluid Dynamic models: CFD-TFM and CFD-DEM. The two models were compared and validated with data from literature, showing good agreement between experimental and simulated results. Both models were able to predict the dynamics of the bed from the static situation to stable spouting conditions, even though some discrepancies in the solid volume fraction or velocity profiles were observed. Overall, CFD-DEM

reproduced better the experimental measurements, and, since the computational effort was proved to be similar in both cases due to the low number of particles in the bed, it was preferred to describe the present spouted bed. In larger systems, however, CFD-DEM might not be so convenient, requiring the evaluation of the degree of accuracy and the computational costs prior to the application of this or alternative models.

1. INTRODUCTION

Spouted Beds (SB) continue to attract interest in recent years for a broad range of applications, mostly related to drying processes, due to the high fluid-solid contact achieved [1]. Spouted beds currently stand out as a promising technology to carry out thermo-chemical reactions such as pyrolysis [2,3], gasification [4,5] and combustion [6,7] of different materials, such as coal or waste products. A Spouted Bed can be described as a conventional fluidisation reactor in which the perforated plate has been replaced by single orifice place, promoting enhanced recirculation of solids with a particular multiphase pattern [8]. Three different regions can be distinguished in a SB: Spout (S), Annulus (A) and Fountain (F), as shown in Figure 1.
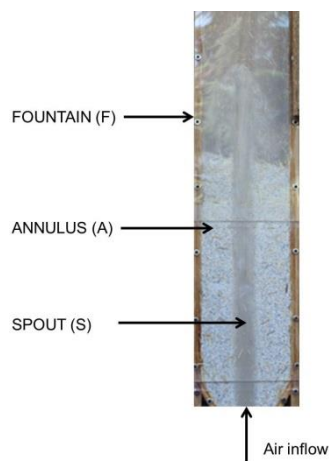

Figure 1. Regions within a SB (System PET/straw 5%v/v; Initial bed height = 50 cm).

The gas enters the bed through a central orifice of the distributor plate, causing the formation of a central spout in which the particles move upwards in a dilute phase. The annular space between the spout and the vessel wall contains a packed bed of particles that moves slowly downwards and radially inwards. The conical base enhances recirculation, enabling the movement of bigger and more irregular particles, and preventing potential stagnant or dead zones. Several devices have

been recently studied to improve further the stability of the bed such as draft tubes [9] and fountain confiners [10] extending their range of application. The scalability of the reactor is of the essence to develop and apply models, as a strategy to optimise geometrical factors and minimise heat losses, investments and operating costs.

CFD modelling has become a powerful tool for the study of multiphase flows based on the development of computational power and the advance of numerical algorithms. Currently, two approaches are mainly applied: the Eulerian-Eulerian approach (Two Fluid Model, CFD - TFM) and the Eulerian-Lagrangian approach (Discrete Element Method, CFD - DEM). CFD-TFM considers both the solid and the gas phases as interpenetrating continua, and is feasible for industrial-scale facilities, even though it is highly sensible to the parameter choice. CFD-DEM, on the other hand, tracks the trajectory of each discrete particle, thus representing the most natural choice, but it is more computationally complex and can be used up to lab-scale devices [11]. It is clear that the main difference between the two approaches is the way solid particles are considered within the simulation. CFD-TFM implicitly calculates any particle – particle interaction using the kinetic theory of granular flows (KTGF) to determine the particle interaction forces. In contrast, in the CFD-DEM model, the particle interactions are explicitly calculated by tracking each particle or number of particles, named parcels.

Both strategies are valid to investigate several systems in industry, including the hydrodynamics of simple [12–14] or complex [15,16] spouted beds and the mixing of heterogeneous particles [17,18]. In the literature, the Eulerian-Lagrangian approach is typically deemed more accurate for the simulation of spouted beds in, for example, works performed with Fluent [19], Fluent and DEMEST [20] and OpenFOAM [21]. Similar conclusions were also drawn by comparing the two approaches on simulations performed for fluidised bed carbonator [22] and a bubbling fluidised bed [23]. Nonetheless, both approaches present advantages and drawbacks, and the establishment of a mature choice for the simulation of spouted beds remains open to discussion.

This paper intends to shed light about the available modelling approaches by comparing the Euler – Euler and Euler – Lagrangian approaches for the single case of a spouted bed. The comparison is based on the experimental data by Zhao et al. [24] and the models are compared in terms of

accuracy, simulation time or number of required variables among others using Ansys Fluent® (ANSYS Inc. Canonsburg, USA). We envisage that the present work will provide with valuable information in terms of general and specific set of equations, set-up of simulations and numerical convergence considerations, and will help us determine the advantages and disadvantages of each modelling approach to simulate spouted beds.

2. NUMERICAL MODEL DESCRIPTION

2.1. Two-Fluid Model (CFD - TFM)

The CFD-TFM approach uses a generalised form of the Navier-Stokes equations, with each phase having its own properties. The fluid and solid phases are treated mathematically as interpenetrating continua and the volume fractions of the overlapping phases are assumed to be continuous functions of space and time. Equivalent conservation equations are used for each phase and additional closure laws are applied to describe particle–particle and particle–fluid interactions, using the kinetic theory of granular flow (KTGF) [25].

o *Governing equations*

The continuity equation for each phase q (g - gas or s - solid) assuming no mass transfer between phases is

$$\frac{\partial}{\partial t}\left(\alpha_q \rho_q\right) + \nabla\left(\alpha_q \rho_q \vec{u}_q\right) = 0$$

Eq. 1

where ρ_q and $\bar{u}_q$ are the density and velocity of phase q respectively and $\alpha_s = 1 - \alpha_g$.

Similarly, the momentum conservation equation for each phase *q* (q = g, s) is

$$\frac{\partial}{\partial t}\left(\alpha_q \rho_q \vec{u}_q\right) + \nabla\left(\alpha_q \rho_q \vec{u}_q \vec{u}_q\right) = -\alpha_q \nabla p + \alpha_q \rho_q (\vec{g} + \vec{F}_q + \vec{F}_{lift,q} + \vec{F}_{vm,q}) + \nabla \vec{\vec{\tau}}_q + \sum_{q=1}^{n} \vec{R}_{pq}$$

Eq. 2

where p is the fluid pressure, $\vec{g}$ is the gravitational acceleration, $\vec{F}_q$ is the external body acceleration, $\vec{F}_{lift,q}$ is the lift acceleration and $\vec{F}_{vm,q}$ is the virtual mass acceleration, $\vec{\vec{\tau}}_q$ is the Reynolds stress tensor and $\vec{R}_{pq}$ is the interaction force between phases.

Lift forces are considered when particle size is relatively large and account for the forces acting on a particle in response to velocity gradients in the air flow field. Virtual mass occurs when a solid phase accelerates relative to the gas phase. In this work, lift forces [26] and virtual mass ($\vec{F}_{vm,q} = 0.5$) were considered together with the drag force (described in detail in Section 2.3) and gravity (g = -9.81 m/s^2).

o *Closure equations*

One set of closure equations regards the *solid-solid momentum exchange* and represents the interfacial forces, solids stress and turbulence in both phases. For this purpose, the *kinetic theory of granular flow* [25] is applied, as an analogy to the well-established kinetic theory of gases.

Figure 2 shows a schematic representation of the two flow regimes that can be distinguished in granular flows. At *high particle concentrations* (bed of the reactor) individual particles interact with the multiple neighbours and normal and tangential *frictional forces* are the major contributions on the particle stresses. At *low particle concentrations*, on the other hand, stresses are mainly caused by particle-particle *collisions* or translational transfer of momentum [27]. The kinetic theory takes both approaches and considers the sum of a rapidly shearing flow regime, in which kinetic contributions are dominant, and a quasi-static flow regime, in which friction is the dominant phenomenon.
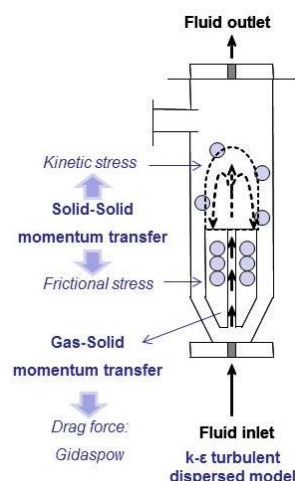

Figure 2. Schematic representation of the flow regimes in granular flows.

As a result, the estimation of the solid stress is defined by the solid "pressure" and "viscosity", included in the general conservation equation (Eq. 3). The concept of granular temperature of the

solids phase, $\Theta_s = \dfrac{u_s^2}{3}$, is introduced as a measure of particle velocity fluctuations, and the conservation equation for the granular phase s is given by

$$\frac{3}{2}\left[\frac{\partial}{\partial t}(\alpha_s \rho_s \Theta_s) + \nabla(\alpha_s \rho_s \Theta_s)\vec{u}_s)\right] = \left(-p_s \cdot \vec{\vec{I}} + \vec{\vec{\tau}}_s\right) : \nabla \vec{u}_s - \nabla(k_{\Theta_s}\nabla \Theta_s) - \gamma_{\Theta_s} + \phi_s \qquad \text{Eq. 3}$$

where $\left(-p_s \cdot \vec{\vec{I}} + \vec{\vec{\tau}}_s\right) : \nabla \vec{u}_s$ is the generation of energy by the solid stress tensor, $k_{\Theta_s}\nabla \Theta_s$ is the diffusion of energy, ϕ_s is the energy exchange between the fluid and solid phases ($\phi_s = -3\beta\Theta_s$) and γ_{Θ_s} is the collisional dissipation of energy

$$\gamma_{\Theta_s} = \frac{12(1 - e_{ss}^2)\alpha_s^2 \rho_s g_0 \Theta_s^{3/2}}{d_p \sqrt{\pi}} \qquad \text{Eq. 4}$$

where e_{ss} is the inter-particle coefficient of restitution (in this work equal to 0.9), a measure of energy dissipation in particle-particle collisions, and g_0 the radial distribution function, defined as a correction factor that modifies the probability of collisions between grains.

The second set of closure equations regards the *gas-solid momentum exchange*, which defines the drag force exerted on particles in fluid-solid systems. These are usually expressed by the product of a momentum transfer coefficient β and the relative velocity ($\vec{u}_g - \vec{u}_s$) between the two phases. This term is a key modelling parameter for the simulation of spouted beds in both approaches and therefore is described in detail in Section 2.3.

2.2. Discrete Element Method (CFD - DEM)

In the Eulerian-Lagrangian approach, the behaviour of the gaseous phase is described similarly as for CFD-TFM, considering the local balances of mass and momentum given in Eq. 1 and 2. The treatment of the solid phase is, however, completely different. The core principle of CFD-DEM is that each particle is considered as a discrete element, and its behaviour is predicted through its Newtonian equations of motion

$$\frac{d\vec{u}_p}{dt} = \frac{\beta(\vec{u} - \vec{u}_p)}{\rho_p} + \vec{g}\frac{\rho_p - \rho}{\rho_p} + \vec{F}_{coll}$$

Eq. 5

$$\frac{d\vec{\omega}_p}{dt} = \frac{15}{16\pi}\frac{\rho}{\rho_p}C_\omega\left(\frac{1}{2}\nabla \times \vec{u} - \vec{\omega}_p\right)$$

Eq. 6

where:

- $\vec{F}_{other}$ is the resulting contact force, generated upon particle-particle or particle-wall interactions.

- β is the gas-solid exchange coefficient, accounting for the drag force, as explained in Section 2.3.

- C_ω is the rotational drag coefficient, which contains the rotational Reynolds number Re_ω, thus expressed by

$$C_\omega = \frac{6.45}{\sqrt{Re_\omega}} + \frac{32.1}{Re_\omega}$$

Eq. 7

$$Re_\omega = \frac{\rho\left(\frac{1}{2}\nabla \times \vec{u} - \vec{\omega}_p\right)d_p^2}{4\mu}$$

Eq. 8

The collisions between particles are evaluated through the so-called 'soft-sphere' approach, in which particles slightly overlap during collisions, by considering the unit vector $\vec{e}_{12}$ and the overlap δ of two colliding particles *1* and *2*

$$\vec{e}_{12} = \frac{\vec{x}_2 - \vec{x}_1}{\|\vec{x}_2 - \vec{x}_1\|}$$

Eq. 9

$$\delta = \|\vec{x}_2 - \vec{x}_1\| - (r_1 + r_2)$$

Eq. 10

with position vectors $\vec{x}_i$ and radius r_i.

The 'spring-dashpot' model only requires the definition of two values: a positive spring constant, K, and a coefficient of restitution for the dashpot term, η (0 < η < 1), which accounts for both the repulsivity and the inelasticity of the collisions, through a linear Hookean force and a dashpot respectively [28]

$$\vec{F}_1 = -\vec{F}_2 = [K\delta + \gamma(\vec{u}_{12} \cdot \vec{e}_{12})]\vec{e}_{12}$$

Eq. 11

in which

$$\vec{u}_{12} = \vec{u}_2 - \vec{u}_1 \qquad\qquad \text{Eq. 12}$$

$$\gamma = -2\frac{m_{12}\ln\eta}{t_{coll}} \qquad\qquad \text{Eq. 13}$$

$$t_{coll} = f_{loss}\sqrt{\frac{m_{12}}{K}} \qquad\qquad \text{Eq. 14}$$

$$m_{12} = \frac{m_1 m_2}{m_1 + m_2} \qquad\qquad \text{Eq. 15}$$

$$f_{loss} = \sqrt{\pi^2 + \ln^2\eta} \qquad\qquad \text{Eq. 16}$$

The force between particles in contact is evaluated through the friction collision law (called 'friction-dshf' in the software). This law is based on the Coulomb friction equation and calculates the friction force ($F_{friction}$) as a product of a friction coefficient (μ_f) and the force normal to the surface (F_{normal})

$$F_{friction} = \mu_f F_{normal} \qquad\qquad \text{Eq. 17}$$

The force has a direction opposite to the relative motion of the two particles, and depends on both the size of the tangential motion and the size of other tangential forces (such as gravity or drag). The friction coefficient depends on the relative tangential velocity magnitude (v_r) and requires the definition of six parameters:

- Sticking friction coefficient (μ_{stick}).
- Gliding friction coefficient (μ_{glide}).
- High velocity limit friction coefficient (μ_{limit}).
- Gliding velocity (v_{glide}): for lower velocity values, the friction coefficient is interpolated between μ_{stick} and μ_{glide}.
- Limit velocity (v_{limit}): for higher velocity values, the friction coefficient approaches μ_{limit}.
- Speed at which the friction coefficient approaches μ_{limit} (slope$_{limit}$).

These parameters are difficult to evaluate experimentally, and this work uses the standard values already present in Fluent alternatively. The equations for the calculation of the friction coefficient, μ_f, are

$$\mu_f = \mu_{stick} + (\mu_{stick} - \mu_{glide})(v_r/v_{glide} - 2.0)\, v_r/v_{glide} \quad \text{if} \quad v_r \leq v_{glide}$$

Eq. 18

$$\mu_f = \mu_{glide} \quad \text{if} \quad v_{glide} < v_r \leq v_{limit}$$

Eq. 19

$$\mu_f = \mu_{glide} \frac{1 + v_{ratio}}{1 + \mu_{ratio} v_{ratio}} \quad \text{if} \quad v_r > v_{limit}$$

Eq. 20

in which:

$$\mu_{ratio} = \mu_{glide}/\mu_{limit}, v_{ratio} = (v_r - v_{limit})/slope_{limit}$$

Eq. 21

2.3. Drag model

We use the Gidaspow drag model [29], which is the widely applied drag model for the simulation of spouted beds [1]. The drag force for the dense phase is calculated by the Ergun equation [30] and the drag force for the dilute phase is calculated by the Wen-Yu expression [31]

$$\beta\big|_{Ergun} = 150 \frac{(1-\alpha_g)^2 \mu_g}{\alpha_g^2 d_p^2} + 1.75 \frac{(1-\alpha_g)\rho_g}{\alpha_g d} \left| \vec{u}_g - \vec{u}_s \right| ; \text{ for the range } \alpha_g < 0.8$$

Eq. 22

$$\beta\big|_{Wen\&Yu} = \frac{3}{4} \frac{(1-\alpha_g)}{d_p} \rho_g C_D \alpha_g^{-2.65} \left| \vec{u}_g - \vec{u}_s \right| ; \text{ for the range } \alpha_g \geq 0.8$$

Eq. 23

where μ_g is the air viscosity, d_p is the particle diameter, $\vec{u}_g$ is the gas velocity, $\vec{u}_s$ is the particle velocity and C_D the drag coefficient, expressed as

$$C_D = \frac{24}{\alpha_g \, \text{Re}} \left(1 + 0.15(\alpha_g \, \text{Re})^{0.687} \right); \text{Re} < 1000$$

Eq. 24

$$C_D = 0.44 \; ; \text{Re} \geq 1000$$

Eq. 25

with Re the Reynolds number

$$\text{Re} = \frac{\rho_g d}{\mu_g} \left| \vec{u}_g - \vec{u}_s \right|$$

Eq. 26

In order to avoid the discontinuity at the boundary condition (α_g = 0.8; α_s = 0.2) between the two equations, a switch function was introduced to obtain a rapid transition between regimes:

$$\varphi_{gs} = \frac{arctg\left[150 \cdot 1.75(0.2 - \alpha_s)\right]}{\pi} + 0.5 \qquad \text{Eq. 27}$$

Thus, the interaction between fluid and particles defining the drag force can be summarised as

$$\beta = \varphi_{gs}\left.\beta\right|_{Wen\&Yu} + (1 - \varphi_{gs})\left.\beta\right|_{Ergun} \qquad \text{Eq. 28}$$

Finally, the value of β is employed in Eq. 3 for CFD-TFM, Eq. 5 for CFD-DEM and Eq. 2 for both approaches, upon evaluation of $\vec{R}_{pq}$

$$\vec{R}_{pq} = \beta(\vec{v}_g - \vec{v}_s) \qquad \text{Eq. 29}$$

3. MODEL SET UP

The modelling methodology is schematised in Figure 3. Firstly, the *geometry* of the reactor was built with the *Design Modeler* tool provided within FLUENT software. This work domain was then discretised into a number of computational cells, *grids or mesh*, in order to approximate the *governing equations* (Section 2) by a system of algebraic expressions at discrete locations in space and time. In this work, discretisation is based on the Finite Volume Method, and the resulting algebraic equations were *solved at each grid point* by iterative methods until a *converged* solution was achieved. The values are obtained at different points by interpolation of the calculated numerical solution between the grid values. Finally, *a post-treatment* step is carried out to analyse the converged solution.
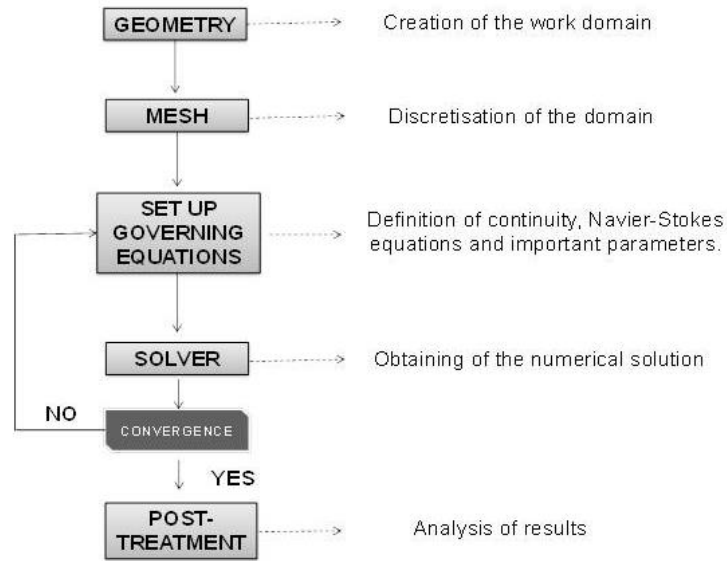
Figure 3. Scheme of the modelling methodology using FLUENT.

3.1. Definition of the device geometry

The apparatus described in Zhao et al. [24] was used in both simulations through representation of their experimental device (considered as pseudo-2D with a width = 15 mm). The schematic view of the geometry and its dimensions are presented in Figure 4, and further details on the experimental conditions can be found in the literature [16].
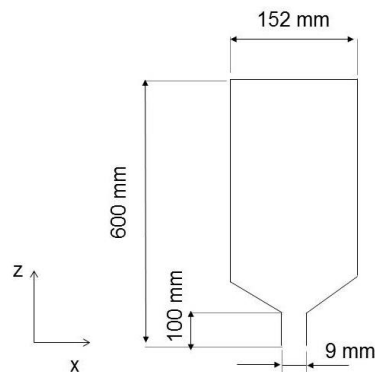

Figure 4. Main dimensions of the spouted bed.

3.2. Definition of mesh

The selection of the grid for CFD calculations strongly influences the accuracy of the solution and also affects the computational work required. In this work, three mesh sizes (d_m/d_p = 3, 4 and 5) were tested to identify the largest mesh size with no significant effect on the results. The number of cells was 8124 (d_m/d_p = 3), 2952 (d_m/d_p = 4, Figure 5) and 2108 (d_m/d_p = 5).
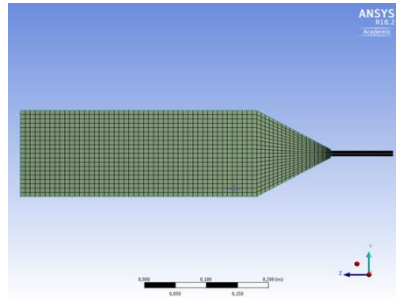

Figure 5. Mesh applied in the simulations using d_m/d_p = 4.

The grid sensitivity was tested by evaluating the CFD results for the three grid sizes. Figure 6 shows the time-averaged volume fraction of glass beads along the bed axis, *z*, for the three different mesh sizes (CFD-TFM) on the spout centre line. Time averaging was performed over the interval 1-2 s to ensure the statistical steady-state behaviour inside the bed. The coarser grid (d_m/d_p ratio=5) led to lower volume fractions in the bed whereas the mid-sized (d_m/d_p ratio=4) and fine grid (d_m/d_p ratio=3) provided the same qualitative trend and reasonable similar quantitative results. The mid-sized mesh (d_m/d_p ratio=4) was then used in subsequent simulations as a compromise between accuracy and computational costs.

Equivalent results were obtained for CFD-DEM simulations, in which the size of the mesh cells must be bigger than the diameter of particles as a general requirement of convergence. In CFD-DEM simulations, the fine grid made the calculations too slow to produce results within acceptable computational times. In a day of calculations, less than 0.1 s of simulation was completed. This happened because the fine mesh required a reduction of the time step to satisfy the Courant-Friedrichs-Lewy (CFL) condition. Moreover, when the ratio d_m/d_p decreases, convergence becomes more difficult and more iterations are required.
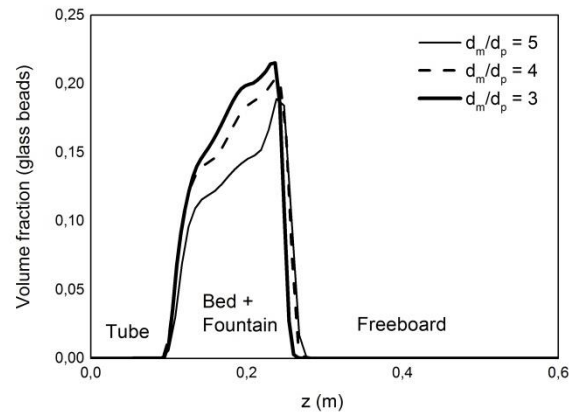
Figure 6. Grid independence test; z = bed axis (spout centre line).

3.3. Materials and definition of bed of particles

The experimental conditions used for the simulations are summarised in Table 1. The bed is composed of glass beads, and it is considered as a static bed (t = 0 s). Air at room temperature is used as fluidising agent, with an inlet velocity of 26.68 m/s along the z axis.

Table 1. Definition of experimental conditions

Parameter	Value	Units
Air density (ρ_g)	1.225	kg/m^3
Air viscosity (μ_g)	$1.7894 \cdot 10^{-5}$	Pa/s
Glass beads density (ρ_p)	2380	kg/m^3
Glass beads diameter (d_p)	0.00203	m
Shape of particles	Spherical	-
Total number of particles	15950	-

The initial height of the bed of particles was set at 10 cm, and the particles were placed inside the reactor in two different ways:

- For the case of CFD – TFM, the solid particles were evenly patched all over the domain with $\alpha_s = 0.65$, Figure 7(a).

- For CFD - DEM simulations, particles settled into the lower part of the reactor through an injection step in absence of air, reaching the desired height, Figure 7(b).
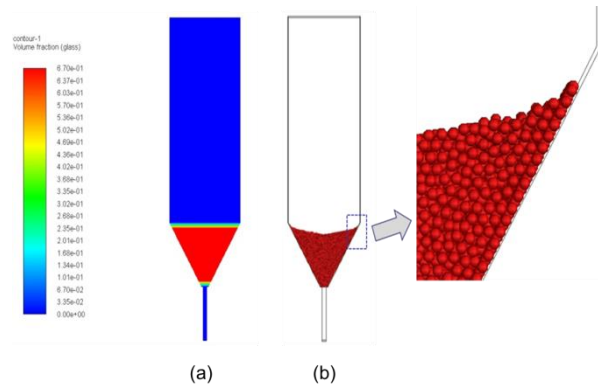
Figure 7. Initial static system at t = 0 s in CFD - TFM (a) and CFD - DEM (b) simulations.

3.4. Physical models

3.4.1. Multiphase modelling

The governing equations were implemented through the *Multiphase model*. For the case of CFD-TFM, two Eulerian phases were considered, including a granular phase (glass beads). CFD-DEM was set by enabling the discrete dense phase model (DDPM), with the Discrete Element Method (DEM) computing the collisions. The selected constitutive equations are presented in Table 2 (CFD-TFM) and Table 3 (CFD-DEM). Their complete description can be found in the Fluent User Guide [32].

Table 2. Constitutive equations and parameters applied to the TFM model.

Granular viscosity	Syamal-O'Brien [21]	Frictional pressure	Based kgtf
Granular bulk viscosity	Lun et al. [17]	Frictional modulus	Derived
Frictional viscosity	Schaeffer [25]	Frictional packing limit	0.5
Angle of friction	28.5 [26]	Granular temperature	Phase property [27]
Radial distribution	Lun et al. [17]	Solids pressure	Lun et al. [17]
Elasticity modulus	derived	Packing limit	0.65

Table 3. Constitutive equations and parameters applied to the DEM model.

Normal contact force law	Spring-dashpot	μ_{glide}	0.2

Tangential contact force law	Friction-dshf		μ_{limit}	0.1
	K	1000 N/m	v_{glide}	1 m/s
	η	0.9	V_{limit}	10 m/s
	μ_{stick}	0.5	$slope_{limit}$	100 s

3.4.2. Turbulence modelling

Turbulence in the gas phase may affect the gas-solid flow behaviour. However, there is no clear consensus on the best turbulence model for CFD simulations of spouted beds and the impact of these fluctuations on the final result. In this work, turbulence was considered using the k-ε dispersed model with a standard wall function as proposed by [33]. The complete set of equations and coefficients applied in the model can be found in [34].

3.5. Boundary and operating conditions

The boundary conditions applied in both simulations were:

- INLET
  - Air inflow = 26.68 m/s.
  - Turbulence intensity = $0.6 \, Re_{dh}^{-1/8}$ = 6.19 %.
  - Hydraulic diameter = $4A/2p$ = 0.01125 m.
- OUTLET
  - Pressure = 0 Pa.
- WALL
  - Gas – No slip.
  - Solid – Specularity coefficient (for CFD-TFM) = 0.4.

3.6. Discretisation equations and calculation parameters

The phase-coupled SIMPLE algorithm is applied for the pressure-velocity coupling. The discretisation schemes were:

- Spatial discretisation

    o Momentum: second-order upwind.

    o Volume fraction: modified HRIC.

    o Turbulence: first-order upwind.

- Time discretisation: first order.

- The values of the under-relaxation factors ranged from 0.2 to 0.7.

The convergence parameters were:

- Scaled residuals: lower than 10^{-3}.

- Time steps:

    o 0.0001 s for CFD – TFM

    o 0.0001 s (fluid phase); $5 \cdot 10^{-5}$ s (discrete phase) for CFD-DEM

- Maximum number of iterations: 35, even though only 5 to 10 iterations were generally required to reach convergence.

All simulations started from a static bed condition. First, 1 s of real life simulation was run to achieve steady state and afterwards the unsteady statistics calculations were activated and the model continued running up to 2 s of real life simulation.

The simulations were carried out using two PCs Intel® Core(TM) i3 CPU 540 @3.07 GHz and 4 Gb RAM.

4. RESULTS AND DISCUSSION

4.1. Particle flow dynamics

Knowledge of gas and particle dynamics is important to evaluate particle circulation rates and gas-solid contacting efficiencies. The simulations of the particle flow patterns from the static situation in

Figure 7 to stable spouting are sequentially represented in Figure 8(a) (CFD-TFM) and 8(b) (CFD-DEM).
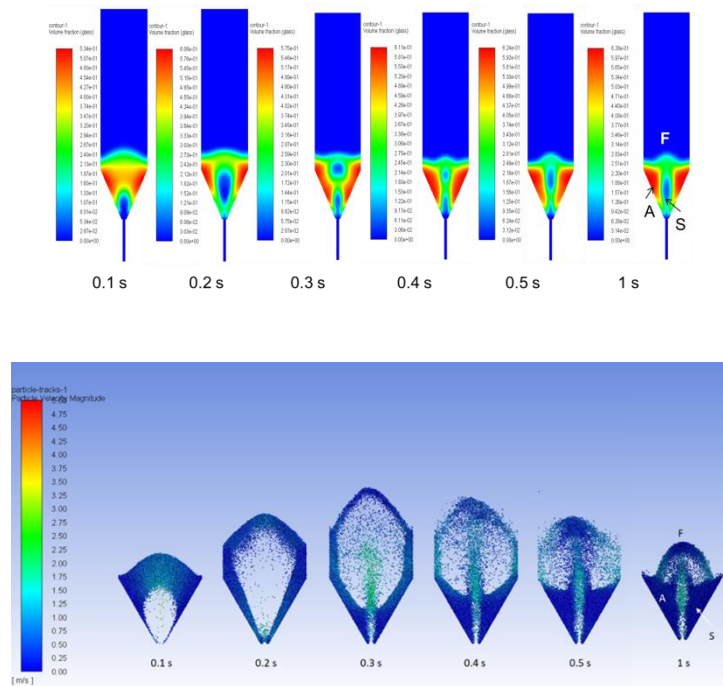

Figure 8. Particle flow patterns at different simulation times, with U_g = 1.58 m/s and H_b = 10 cm: CFD-TFM (a) and CFD-DEM (b).

The overall *solid flow patterns* within the spouted bed were predicted well by the two models, *i.e.* the stable spout region (S), the fountain region (F) and the annular down-comer region (A). The system moves away from its static situation (Figure 6) when the fluidising agent enters the bed (u_y = 26.68 m/s, corresponding to U_g = 1.58 m/s as reported experimentally) and opens its way through the cavity. At 0.1 s, a marked neck is shown which propagates upwards (0.2, 0.3 s) and finally disappears when reaching the bed surface (0.4 s).

When reaching the surface, the particles are scattered between the annulus forming the so-called fountain, and reaches steady spouting regime at 0.5 s. The *diameter of the spout* increases when moving up through the bed, regardless of the modelling approach, and in consistence with typical spout shapes [35]. The system reaches stationary conditions after 1 s. This behaviour fully agrees with the experimental data in which the PIV profiles showed a regular spouting of particles after 0.5 s.

As it was expected, the representations of the two simulated sequences in Figure 8 show different degrees of detail. More precisely, since CFD-DEM calculates the particles movements individually, the graphical representation of the system becomes more realistic and the trajectory of solids can be easily tracked [36]. This feature becomes particularly interesting to observe the distribution of solids if mixtures are used in the beds, and would help detect eventual segregation problems easily [37]. With CFD-TFM, on the contrary, it is not possible to obtain accurate solid distributions, since solids are considered as fluids.

4.2. Particle velocity profiles

Figure 9 shows the predicted (full line) and experimental (empty symbols) *time-averaged particle velocity profiles*, v_z, on the spout centreline for (a) CFD-TFM and (b) CFD-DEM (with the equivalent contour representation as the inset). Both velocity profiles can be divided into three differentiated parts: an initial increasing zone (I), a 'plateau' (II) and a decreasing zone (III). In short, in the increasing zone, particles accelerate due to the high gas velocity close to the inlet, and decelerate as they displace through the z axis of the reactor, essentially due to gravity. Similar trends for the velocity profile of particles in the spout were reported in previous references [24] as well as in experimental works [38], which further validates the obtained results.
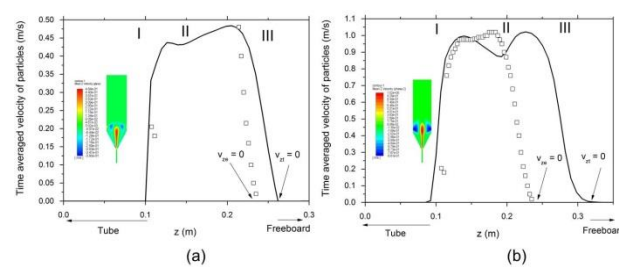

(a)   (b)

Figure 9. Profile of the averaged particles vertical velocity, v_z, on the spout centreline (a) CFD-TFM and (b) CFD-DEM (Inset: equivalent contour representation). *z*, vertical reactor axis (full line: simulation results; empty symbols: experimental data).

Both approaches predict the experimental behaviour qualitatively: after the end of the inlet tube, particles are rapidly accelerated and reach the maximum velocity: this value is more or less constant in a zone that is longer than the original static bed. Then, at the end of the fountain, particles rapidly

decelerate. In both plots, the particles velocity never reaches negative values, as experimentally reported. The shape predicted in the plots is similar for both approaches, but CFD-TFM underestimates the maximum velocity (which is about 1 m/s experimentally) whereas CFD-DEM provides with a good approximation. CFD-TFM is instead more accurate at predicting the fountain height: simulations yielded a value of about 150 mm above the end of the tube (z at which $v_{zt} = 0$ in Figure 9a), while the experimental value is 135 mm (z at which $v_{ze} = 0$),. CFD-DEM simulations, on the other hand, over predicted the fountain height, with a value of about 200 mm (z at which $v_{zt} = 0$ in Figure 9b),.

Figure 10 displays the predicted (full lines) and experimental (empty symbols) radial profiles of the vertical particle velocities in the spout. Individual particles are rapidly accelerated near the center axis until a maximum value, after which the particle velocities gradually decelerate. The local vertical particle velocity decreases with an increase in radial distance from the spout axis. Again, CFD-TFM underestimates the velocity values and presents a slower deceleration trend for all heights, see Figure 10(a) , whereas CFD-DEM predicts well the profiles in all cases, Figure 10(b).
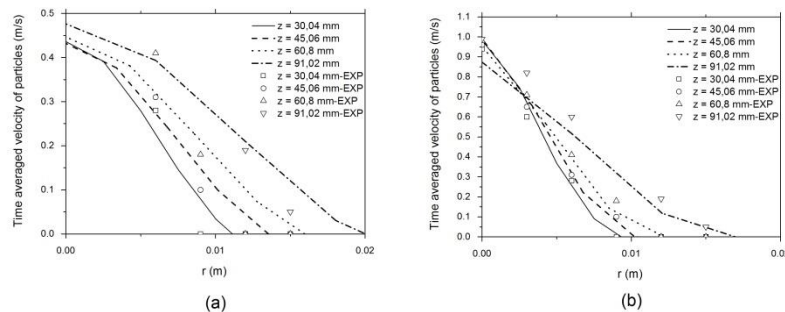

Figure 10. Radial profile of the averaged particles velocity, v_z, at different heights for (a) CFD-TFM and (b) CFD-DEM (full line: simulation results; empty symbols: experimental data).

The *averaged solid velocity vectors* are shown in Figure 11 for the CFD-DEM model. A fast particle motion in the spout zone (range 0.8-1 m/s) and the typical cyclic movement of solids can be easily observed, in agreement with the literature [24]. Particles from the spout move downward in the fountain and then fall into the annulus. Near the gas inlet, particles move from the annulus to the spout and are carried up by the gas through the spout repeating the cycle again. In addition, solid cross-flow can be identified (inset in Figure 11), which can be useful to evaluate the preferential solid

flow paths within the spouted. Figure 12 depicts the instantaneous velocity vectors after 5 seconds

of simulations. As it was expected, the overall pattern is almost identical to the average profile, but

there are some asymmetry effects that are absent in Figure 11, due to time-averaging.
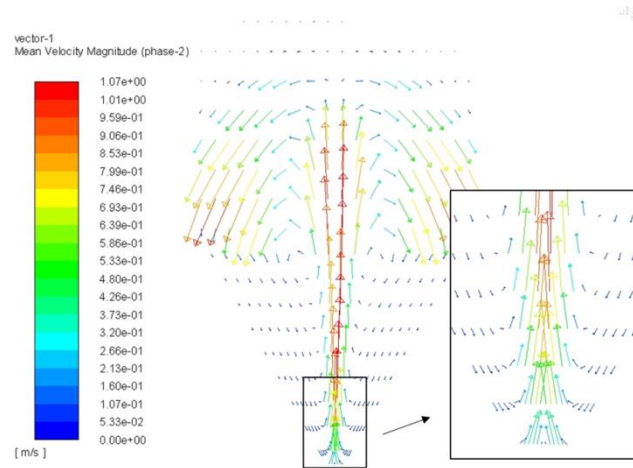

Figure 11. Averaged solid velocity vectors for CFD-DEM (Inset: solid-cross flow).
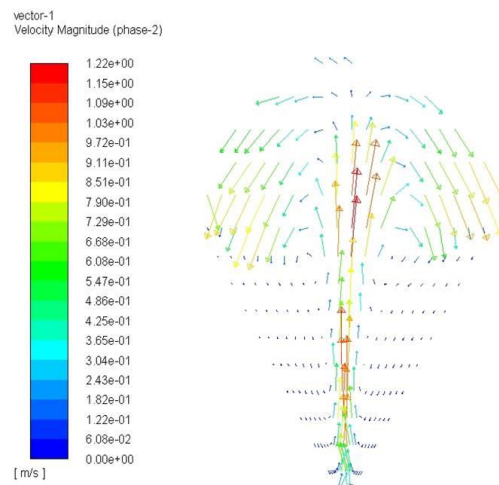
Figure 12. Instantaneous solid velocity vectors for CFD-DEM, at t = 5 s.

The *height of the fountain* can be obtained from Figures 9 and 11, as the z value at which the velocity

of solids equals zero, giving 16 cm for CFD-TFM, and 20 cm CFD-DEM, the latter correlating well

with the experimental value of 13.5 cm as previously discussed.

The *granular temperature* represents the particle velocity fluctuation using a model analogue to the

kinetic theory of granular flow (Section 2), and was calculated from the CFD-TFM simulations, see

Figure 13. As expected, the instantaneous granular temperature increases in the spout zone near the inlet due to the low concentration and high velocity of particles, and decreases in the annulus region due to the high concentration and low velocity of particles. In the fountain zone, the granular temperature exhibits an intermediate value among the two previously described zones. These results are in good agreement with previous CFD works [39]. It is worth noting that this parameter could not be calculated from the CFD-DEM simulations.
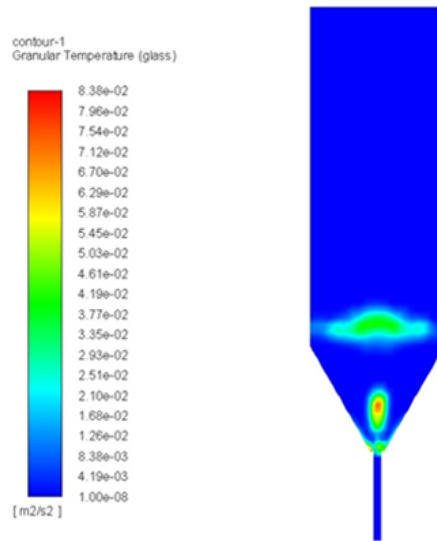

Figure 13. Instantaneous granular temperature distribution (t = 2 s).

4.3. CPU cost

For the selected mesh sizes, the required computational time to simulate 1 second of real spouting was 150 min for CFD-TFM, and 200 min for CFD-DEM. These are similar values, which can be explained by the small number of particles in the system. In this scenario, CFD-DEM becomes a more efficient tool, providing more detailed information regarding the system at comparable time costs. Moreover, some post-processing analysis can only be performed on CFD-DEM simulations, such as the calculation of the solids circulation rate, as it was mentioned earlier.

It should be pointed out that the computational complexity of CFD-DEM simulations increases exponentially with the number of particles. This might make CFD-DEM inviable for some approaches, such as systems containing very small particles or industrial-scale devices. Conversely, TFM simulations are not dependent on the total number of entailed particles. In CFD-DEM

simulations, it is possible to partially overcome this problem through the so-called coarse-graining method. This method employs parcels, which are computational particles with sizes that differ from those of the experimental particles. By employing parcels that lump several particles, it is possible to reduce the total number of tracked elements and speed up the simulations. This is a common procedure, which can produce reliable results [13,15,22]. Nonetheless, the use of coarse parcels results in a coarse mesh, because the size of the parcels must be smaller than that of each cell. Thus, this approach might not always be applicable, as a coarse mesh might result in a poor prediction of the gas phase behaviour. This is especially valid when the diameter of physical particles is already high. Due to the small number of particles, the coarse-graining approach was not necessary for this work.

4.4. Comparison of modelling approaches

Table 4 summarises the main advantages and disadvantages of each of the modelling approaches discussed along the manuscript.

The models are governed by different equations, and have common (drag and turbulence models, restitution coefficients) and exclusive (*i.e.* spring constant for CFD-DEM or granular temperature for CFD-TFM) parameters. On this basis, we could argue that the Two Fluid Model requires more fitting parameters to obtain an accurate solution whereas the Discrete Element Method relies on fewer numerical assumptions. The post-processing analysis is also affected by the differences in the fundamental equations. Solid trajectories or circulation rates are only calculated by CFD-DEM , whereas granular temperature is exclusively obtained by CFD-TFM. In any case, an adequate choice of the fitting parameters (specularity or restitution coefficient) is crucial to obtain accurate results, particularly in CFD-TFM.

Overall, the simulations on our system showed that CFD-DEM is more accurate than CFD-TFM, providing more detailed results with similar computational times and using common settings. Further refining of the CFD-TFM model varying these settings (i.e. drag law, turbulence model, restitution coefficient) and refinement of the mesh (it was fixed to a cell size of 8 mm for both cases) should improve the outcomes.

Lastly, our system consisted of particles with averaged size, and comprised a moderate number of particles. In most real-scale applications, billions of multi-dispersed particles could be present, and at the moment this poses several problems for the widespread usage of CFD-DEM, in terms of constraints on the mesh size and computational time. More efforts to overcome these limitations are needed, making CFD-TFM the first choice for many industrial applications, despite some of its inherent drawbacks that have been evidenced in the present work.

Table 4. Advantages and disadvantages of the modelling approaches.

	Advantage	Disadvantage
CFD – TFM	Relatively smaller CPU and memory resource requirements: efficient simulation of larger scale systems. Computational requirements depend on mesh size and not on particle diameter: possibility of using models with the largest independent mesh.	Greater number of parameters needs to be fitted for an accurate solution. Some post-processing analysis cannot be performed (*i.e.* calculation of solids circulation time and rate, particle trajectories).
CFD - DEM	It requires fewer assumptions and therefore provides more realistic solutions. The system can be fully described through the calculation of all the defining variables.	Computational requirements depend on number and dimension of particles: high number of particles leads to computationally intensive systems limited by computational power. Minimum size of mesh limited by parcel dimensions.

5. CONCLUSIONS

A spouted bed was simulated through two Computational Fluid Dynamic models: CFD-TFM and CFD-DEM. The models were validated by comparison with experimental data reported by Zhao et al. [24], showing good agreement between experimental and simulated results.

Both models were able to predict the dynamics of the bed from the static situation to stable spouting conditions. However, discrepancies in the solid volume fraction and the velocity profiles were reported, and, in general terms, the CFD-DEM model reproduced more accurately the spouted bed

performance. The computational effort was proved to be similar in both cases due to the low number of particles in the bed.

In conclusion, we believe that the CFD-DEM model is the most adequate to describe the present spouted bed. CFD-TFM, however, might be more convenient for larger and more complex systems, and the evaluation of the degree of accuracy and the computational costs will always be necessary when opting for a certain simulation strategy.

Nomenclature

A area [m^2]

a volume fraction [-]

C_D drag coefficient [-]

C_ω rotational drag coefficient [-]

d_m size of the mesh cells [mm]

d_p particle diameter [mm]

e_{ij} unit vector for parcels i and j [-]

e_{ss} particle-particle restitution coefficient [-]

F_i collision force acting on particle i [N]

$F_{lift,q}$ lift acceleration [m/s^2]

F_{other} resulting acceleration of external forces acting on a particle [m/s^2]

F_q external body acceleration [m/s^2]

$F_{vm,q}$ virtual mass acceleration [m/s^2]

f_{loss} loss factor [-]

g gravitational acceleration [m/s^2]

g_0 radial distribution function [-]

I   identity tensor [-]

K   spring-dashpot constant [N/m]

$k_{\Theta s}$ diffusion coefficient for the granular energy [kg/(m·s)]

m   mass of a particle [kg]

m_{ij} reduced mass for parcels i and j [kg]

p   pressure [Pa]

Q   gas volumetric rate [m^3/h]

R_{pq} interaction force between the gas and solid phases [N/m^3]

Re   Reynolds number [-]

Re_{dh} Reynolds number calculated with the hydraulic diameter [-]

Re_{ω} rotational Reynolds number [-]

r_i radius of particle i [m]

$slope_{limit}$ Speed at which the friction coefficient approaches μ_{limit} [-]

t   time [s]

t_{coll} collision time scale [s]

u   fluid phase velocity [m/s]

u_p parcel velocity [m/s]

u_{ij} relative velocity for parcels i and j [m/s]

v_{glide} gliding velocity [m/s]

v_{limit} limit velocity [m/s]

v_r relative tangential velocity magnitude between two particles [m/s]

x_i position vector of parcel i [m]

2p   perimeter [m]

Greek Symbols

β gas-solid exchange coefficient [kg/(m^3·s)]

γ damping coefficient [-]

$\gamma_{\Theta s}$ collisional dissipation of energy [Pa/s]

Δt CFD time step [s]

Δt_{DEM} DEM time step [s]

δ parcels overlap [m]

η dashpot term [-]

Θ_s granular temperature [m^2/s^2]

μ dynamic viscosity of the fluid [Pa·s]

μ_f friction coefficient [-]

μ_{glide} gliding friction coefficient [-]

μ_{limit} high velocity friction coefficient [-]

μ_{stick} sticking friction coefficient [-]

ν kinematic viscosity of the fluid [m^2/s]

ρ density [kg/m^3]

τ_q Reynolds stress tensor [Pa]

φ_{gs} switch function [-]

ϕ_s energy exchange between fluid and solid phases [Pa/s]

ω_p parcel rotational velocity [rad/s]

Subscripts

g   relative to the gas phase

p   particle

q   generic continuum phase

s   relative to the solid phase

Captions

Figure 1. Regions within a SB (System PET/straw 5%v/v; Initial bed height = 50 cm).

Figure 2. Schematic representation of the flow regimes in granular flows.

Figure 3. Scheme of the modelling methodology using FLUENT.

Figure 4. Main dimensions of the spouted bed.

Figure 5. Mesh applied in the simulations using $d_m/d_p = 4$.

Figure 6. Grid independence test; z = bed axis.

Figure 7. Initial static system at t = 0 s in CFD - TFM (a) and CFD - DEM (b) simulations.

Figure 8. Particle flow patterns at different simulation times, with U_g = 1.58 m/s and H_b = 10 cm:

CFD-TFM (a) and CFD-DEM (b).

Figure 9. Profile of the averaged particles vertical velocity, v_z, on the spout centreline (a) CFD-TFM

and (b) CFD-DEM (Inset: equivalent contour representation). *z*, vertical reactor axis.

Figure 10. Radial profile of the averaged particles velocity, v_z, at different heights for (a) CFD-TFM and (b) CFD-DEM.

Figure 11. Averaged solid velocity vectors for CFD-DEM (Inset: solid-cross flow).

Figure 12. Instantaneous solid velocity vectors for CFD-DEM, at t = 5 s.

Figure 13. Instantaneous granular temperature distribution (t = 2 s).

6. BIBLIOGRAPHY

[1]   C. Moliner, F. Marchelli, B. Bosio, E. Arato, Modelling of Spouted and Spout-Fluid Beds: key for their successful scale up, Energies. 10 (2017) 38. doi:10.3390/en10111729.

[2]   A. Arregi, M. Amutio, G. Lopez, M. Artetxe, J. Alvarez, J. Bilbao, M. Olazar, Hydrogen-rich gas production by continuous pyrolysis and in-line catalytic reforming of pine wood waste and HDPE mixtures, Energy Convers. Manag. 136 (2017) 192–201. doi:10.1016/j.enconman.2017.01.008.

[3]   J. Alvarez, B. Hooshdaran, M. Cortazar, M. Amutio, G. Lopez, F.B. Freire, M. Haghshenasfard, S.H. Hosseini, M. Olazar, Valorization of citrus wastes by fast pyrolysis in a conical spouted bed reactor, Fuel. 224 (2018) 111–120. doi:10.1016/j.fuel.2018.03.028.

[4]   D. Bove, C. Moliner, M. Curti, M. Baratieri, B. Bosio, G. Rovero, E. Arato, Preliminary Tests for the Thermo-Chemical Conversion of Biomass in a Spouted Bed Pilot Plant, Can. J. Chem. Eng. (2018). doi:10.1002/cjce.23223.

[5]   A. Niksiar, B. Nasernejad, Activated carbon preparation from pistachio shell pyrolysis and gasification in a spouted bed reactor, Biomass and Bioenergy. 106 (2017) 43–50. doi:10.1016/j.biombioe.2017.08.017.

[6]   M.J. San José, S. Alvarez, R. López, Catalytic combustion of vineyard pruning waste in a conical spouted bed combustor, Catal. Today. 305 (2018) 13–18.

doi:10.1016/j.cattod.2017.11.020.

[7]   M.J. San José, S. Alvarez, I. García, F.J. Peñas, F.J.P. María J. San José, Sonia Alvarez, Iris García, Conical spouted bed combustor for clean valorization of sludge wastes from paper industry to generate energy, Chem. Eng. Res. Des. 92 (2014) 672–678. doi:http://dx.doi.org/10.1016/j.cherd.2014.01.008.

[8]   N. Epstein, J.R. Grace, Spouted and Spout-Fluid Beds, Cambridge University Press, Cambridge, 2010. doi:10.1017/CBO9780511777936.

[9]   J. Makibar, A.R. Fernandez-Akarregi, L. Díaz, G. Lopez, M. Olazar, Pilot scale conical spouted bed pyrolysis reactor: Draft tube selection and hydrodynamic performance, Powder Technol. 219 (2012) 49–58. doi:10.1016/j.powtec.2011.12.008.

[10]   A. Pablos, R. Aguado, M. Tellabide, H. Altzibar, F.B. Freire, J. Bilbao, M. Olazar, A new fountain confinement device for fluidizing fine and ultrafine sands in conical spouted beds, Powder Technol. 328 (2018) 38–46. doi:10.1016/j.powtec.2017.12.090.

[11]   X. Bao, W. Du, J. Xu, An overview on the recent advances in computational fluid dynamics simulation of spouted beds, Can. J. Chem. Eng. 91 (2013) 1822–1836. doi:10.1002/cjce.21917.

[12]   L.W. Rong, J.M. ZHAN, Improved DEM-CFD model and validation: A conical-base spouted bed simulation study, J. Hydrodyn. 22 (2010) 351–359. doi:10.1016/S1001-6058(09)60064-0.

[13]   F. Marchelli, D. Bove, C. Moliner, B. Bosio, E. Arato, Discrete element method for the prediction of the onset velocity in a spouted bed, Powder Technol. 321 (2017) 119–131. doi:10.1016/j.powtec.2017.08.032.

[14]   S. Şentürk Lüle, U. Colak, M. Koksal, G. Kulah, CFD Simulations of Hydrodynamics of Conical Spouted Bed Nuclear Fuel Coaters, Chem. Vap. Depos. 21 (2015) 122–132. doi:10.1002/cvde.201407150.

[15] S. Pietsch, S. Heinrich, K. Karpinski, M. Müller, M. Schönherr, F. Kleine Jäger, CFD-DEM

modeling of a three-dimensional prismatic spouted bed, Powder Technol. (2016).

doi:10.1016/j.powtec.2016.12.046.

[16] S.H. Hosseini, G. Ahmadi, M. Olazar, CFD study of particle velocity profiles inside a draft

tube in a cylindrical spouted bed with conical base, J. Taiwan Inst. Chem. Eng. 45 (2014)

2140–2149. doi:10.1016/j.jtice.2014.05.027.

[17] B. Ren, Y. Shao, W. Zhong, B. Jin, Z. Yuan, Y. Lu, Investigation of mixing behaviors in a

spouted bed with different density particles using discrete element method, Powder Technol.

222 (2012) 85–94. doi:10.1016/j.powtec.2012.02.003.

[18] W. Du, J. Zhang, S. Bao, J. Xu, L. Zhang, Numerical investigation of particle mixing and

segregation in spouted beds with binary mixtures of particles, Powder Technol. 301 (2016)

1159–1171. doi:10.1016/j.powtec.2016.07.071.

[19] A. Stroh, F. Alobaid, M.T. Hasenzahl, J. Hilz, J. Str??hle, B. Epple, Comparison of three

different CFD methods for dense fluidized beds and validation by a cold flow experiment,

Particuology. 29 (2016) 34–47. doi:10.1016/j.partic.2015.09.010.

[20] N. Almohammed, F. Alobaid, M. Breuer, B. Epple, A comparative study on the influence of

the gas flow rate on the hydrodynamics of a gas–solid spouted fluidized bed using Euler–

Euler and Euler–Lagrange/DEM models, Powder Technol. 264 (2014) 343–364.

doi:10.1016/j.powtec.2014.05.024.

[21] S. Golshan, B. Esgandari, R. Zarghami, CFD-DEM and TFM Simulations of Spouted Bed,

Chem. Eng. Trans. 57 (2017) 1249–1254. doi:10.3303/CET1757209.

[22] A. Nikolopoulos, A. Stroh, M. Zeneli, F. Alobaid, N. Nikolopoulos, J. Ströhle, S. Karellas, B.

Epple, P. Grammelis, Numerical investigation and comparison of coarse grain CFD – DEM

and TFM in the case of a 1 MWth fluidized bed carbonator simulation, Chem. Eng. Sci. 163

(2017) 189–205. doi:10.1016/J.CES.2017.01.052.

[23]   J. Le Lee, E.W.C. Lim, Comparisons of Eulerian-Eulerian and CFD-DEM simulations of mixing behaviors in bubbling fluidized beds, Powder Technol. 318 (2017) 193–205. doi:10.1016/J.POWTEC.2017.05.050.

[24]   X.L. Zhao, S.Q. Li, G.Q. Liu, Q. Yao, J.S. Marshall, DEM simulation of the particle dynamics in two-dimensional spouted beds, Powder Technol. 184 (2008) 205–213. doi:10.1016/j.powtec.2007.11.044.

[25]   C.N. Lun C.K.K., Savage S.B., Jeffrey D.J., Kinetic theories for granular flow: inelastic particles in Couette flow and slightly inelastic particles in a general flowfieldNo Title, J. Fluid Mech. 140 (1984) 223–256.

[26]   P.G. Saffman, The lift on a small sphere in a slow shear flow, J. Fluid Mech. 22 (1965) 385–398.

[27]   C. C.S., Granular material flows – an overview, Powder Technol. 162 (2006) 208–229.

[28]   ANSYS, Chapter 24: Modeling Discrete Phase, in: ANSYS FLUENT User's Guid., ANSYS, 2015.

[29]   D. Gidaspow, Multiphase flow and fluidisation, San Diego: Academic Press, 1994.

[30]   S. Ergun, Fluid Flow Through Packed Columns, Chem. Eng. Prog. 48 (1952) 89–94.

[31]   C.Y. Wen, Y.H. Yu, A generalized method for predicting the minimum fluidization velocity, AIChE J. 12 (1966) 610–612. doi:10.1002/aic.690120343.

[32]   ANSYS, ANSYS FLUENT Guide, 2015.

[33]   D. W., Computational Fluid Dynamics (CFD) modeling and scaling up studies of sputed beds, China Univ. Pet. Beijing, China. (2006).

[34]   ANSYS, Chapter 17: Multiphase Flows, in: ANSYS FLUENT Theory Guid., ANSYS, 2015.

[35]   M. Olazar, G. Lopez, H. Altzibar, A. Barona, J. Bilbao, One-dimensional modelling of conical

spouted beds, Chem. Eng. Process. Process Intensif. 48 (2009) 1264–1269. doi:10.1016/j.cep.2009.05.005.

[36]   F. Marchelli, C. Moliner, B. Bosio, E. Arato, A CFD–DEM study of the behaviour of single-solid and binary mixtures in a pyramidal spouted bed, Particuology. (2018). doi:10.1016/j.partic.2018.03.017.

[37]   C. Moliner, F. Marchelli, M. Curti, B. Bosio, G. Rovero, E. Arato, Spouting behaviour of binary mixtures in square-based spouted beds, Particuology. (2018). doi:10.1016/j.partic.2018.01.003.

[38]   M. Olazar, M.J. San José, M.A. Izquierdo, A. Ortiz De Salazar, J. Bilbao, Effect of operating conditions on solid velocity in the spout, annulus and fountain of spouted beds, Chem. Eng. Sci. 56 (2001) 3585–3594. doi:10.1016/S0009-2509(01)00022-7.

[39]   W.Z. S.H. Hosseini, G. Ahmadi, B. S. Razavi, Computational Fluid Dynamic Simulation of Hydrodynamic Behaviour in a Two-Dimensional Conical Spouted Bed, Energy&Fuels. 24 (2010) 6086–6098.

ACKNOWLEDGMENTS